

NANOCRYSTALLINE HIGH ENTROPY MATERIALS: PROCESSING CHALLENGES AND PROPERTIES

Deformation behavior of nanocrystalline and ultrafine-grained CoCrCuFeNi high-entropy alloys

Seungjin Nam¹, Jun Yeon Hwang², Jonggyu Jeon³, Jihye Park⁴, Donghyun Bae³ , Moon J. Kim⁵, Jae-Hun Kim^{1,a)}, Hyunjoo Choi^{1,b)} ¹School of Materials Science and Engineering, Kookmin University, Seoul 02707, Republic of Korea²Institute of Advanced Composite Materials, Korea Institute of Science and Technology, Jeonbuk 55324, Republic of Korea³Department of Materials Science and Engineering, Yonsei University, Seoul 03722, Republic of Korea⁴High Temperature Energy Materials Research Center, Korea Institute of Science and Technology, Seoul 02792, Republic of Korea⁵Department of Materials Science and Engineering, The University of Texas at Dallas, Richardson, Texas 75080, USA^{a)}Address all correspondence to these authors. e-mail: jaehunkim@kookmin.ac.kr^{b)}e-mail: hyunjoo@kookmin.ac.kr

Received: 22 August 2018; accepted: 23 November 2018

Nanocrystalline (NC) and ultrafine-grained (UFG) CoCrCuFeNi high-entropy alloy (HEA) with grain size ranging between 59 and 386 nm was produced via powder metallurgy and heat treatment. The as-sintered HEA exhibited two face-centered cubic (FCC) phases (CoCrFeNi-rich and Cu-rich phases) and a small grain size (59 nm), whereas the alloy after heat treatment at 1000 °C exhibited a CoCuFeNi-rich phase with FCC structure and relatively larger grain size (386 nm). Moreover, the yield strength decreased from 1930 to 883 MPa, and plastic strain to failure increased by 8–32%. In terms of microstructural evolution, grain boundary strengthening coupled with lattice distortion was the dominant strengthening mechanism for NC HEAs. Furthermore, the coefficient for boundary strengthening was higher in the HEAs than in the corresponding pure elemental metals with FCC structure, possibly because of significant lattice distortion. The UFG HEAs exhibited high strength and good ductility because of the activation of dislocation.

Introduction

High-entropy alloys (HEAs), which are multicomponent alloys composed of multiple elements, have widely been investigated for their outstanding mechanical properties and thermal/electrical stabilities [1]. Although HEAs generally exhibit great strength that mainly arises from the significant lattice distortion induced by atomic size differences among alloying elements, they also exhibit a wide range of strengths depending on their composition [2, 3]. For CoCrCuFeNi-based alloys, a number of studies have been performed regarding the compositional effect on microstructural evolution (i.e., phase transformation and/or second phase precipitation) and other resulting properties [4, 5, 6]. In casting materials, CoCrCuFeNi HEAs exhibit yield strength of 230 MPa, which increases to 700 MPa upon the addition of Ti [4]. The addition of elements with large atomic size (e.g., Al, Si, Ti) can significantly increase the degree of solid solution hardening [5, 7]. The Vickers hardness of $\text{Al}_x\text{CoCrCuFeNi}$ alloys [5] increased from approximately 130 to 210 Hv with increasing Al content without phase transformation until $x = 0.5$.

Furthermore, when the Al concentration exceeded $x = 0.5$, the hardness significantly increased due to the phase transformation from a face-centered cubic (FCC) to body-centered cubic (BCC) structure. The formation of hard second phases (e.g., Sigma phase and Laves phase) in HEAs causes additional strengthening by precipitation hardening [8, 9]. The addition of Mo to the CoCrFeNi HEA increased the strength from 155 to 815 MPa due to precipitation of the Sigma phases [9].

On the other hand, nanocrystalline (NC; grain size, $d: d < 100$ nm) or ultrafine-grained (UFG; grain size: $100 \text{ nm} < d < 1 \mu\text{m}$) HEAs have been used in the development of ultra-high-strength materials, where the strength of the crystalline materials is dramatically enhanced with microstructural refinement to the nanoscale [10, 11]. Generally, NC and/or UFG materials are produced via severe plastic deformation (SPD) and powder metallurgy (P/M) [12, 13, 14, 15]. For SPD processes, high-pressure torsion (HPT) and equal-channel angular pressing (ECAP) are employed to refine the microstructure of HEAs by introducing a strong shear force into the

materials [16, 17, 18]. CoCrFeMnNi HEA produced by HPT exhibits a grain size and nanoindentation hardness of approximately 40 nm and 6.2 GPa, respectively [16]. Moreover, the yield strength of CoCrFeMnNi HEA increased from 240 to 980 MPa with increasing ECAP pass number because of the refined microstructures [18]. For P/M, on the other hand, mechanical alloying is considered to be a useful method for synthesizing nanostructured alloys [19, 20]. Multicomponent powders are uniformly mixed at the atomic level during ball milling, and the microstructures are significantly refined by the high impact energy of the balls [21]. Al_{7.5}Co₂₅Cu_{17.5}Fe₂₅Ni₂₅ and Al_{0.15}CoCrCuFeNi HEAs produced by high-energy ball milling followed by sintering showed high yield strengths of 1795 and 2047 MPa, respectively, due to the nanostructure with average grain sizes of 95 and 167.2 nm, respectively [14, 22].

Although the nanostructured microstructures effectively enhance the strength of crystalline metals, plastic deformation is limited because of their inability to accumulate dislocations inside the nanoscale grains and the high residual stress [23, 24]. It is well known that the poor elongation of NC/UFG materials can be recovered by annealing due to strain relaxation. Sun et al. investigated the microstructural and mechanical evolution as a function of annealing temperature in UFG CoCrFeMnNi HEAs produced via casting followed by cold rolling [25]. Full recrystallization in the HEA annealed at 650 °C resulted in an ideal balance between strength and elongation. Even though the material ductility was enhanced by annealing at high temperatures, decreased strength was observed as part of the well-known strength–ductility trade-off. However, this trend may differ in NC HEAs prepared using conventional metals or alloys because of their unique microstructural features based on significantly distorted lattices of multiple elements [26, 27, 28]. Nevertheless, the effect of grain size on deformation behavior has rarely been studied in NC HEA materials.

In this study, we investigated the microstructural evolution and mechanical properties after heat treatment of NC CoCrCuFeNi HEAs prepared by mechanical alloying followed by spark plasma sintering (SPS) at various temperatures. First, microstructural changes (e.g., grain size, phase) of the ball-milled HEAs and heat-treated pallets were examined after varied milling durations and heat treatment temperatures. Subsequently, the strengthening and deformation behaviors of NC and UFG CoCrCuFeNi HEAs are discussed with consideration of the volume fraction and composition of each phase along with grain size.

Results

Phase evolution after ball milling, sintering, and heat treatment

Figure 1(a) shows the X-ray diffraction (XRD) patterns of the Co–Cr–Cu–Fe–Ni powders ball milled for 24, 48, 72, 96, and

120 h. Powders after less than 72 h of milling exhibited peaks corresponding to FCC and BCC phases regardless of milling time, while a single FCC phase was observed after milling for >96 h. During milling, the high impact energy of the balls on the mixed elemental powder induces repeated flattening and cold welding, forming lamellar structures and accelerating atomic diffusion at the interface between lamella. This process results in atomic-level alloying and the formation of a metastable phase [29]. Hence, the single FCC phase, which is predicted to be observed in an equiatomic CoCrCuFeNi alloy according to the phase formation rule for HEAs [30, 31], was formed after ball milling the mixed powder for >96 h. Based on the XRD analysis, the 120-h milled powder was selected for further processing to ensure the finest microstructure and compositional homogeneity. Figure 1(b) shows the XRD of an as-sintered HEA pallet and the samples after heat treatment at 400, 600, 800, and 1000 °C. After sintering, the single phase was separated into two FCC phases with different lattice parameters (i.e., 3.586 and 3.615 Å for FCC 1 and 2, respectively) and Cr oxides were newly formed. While the patterns of CoCrCuFeNi HEAs after heat treatment at 400, 600, and 800 °C were similar to that of the as-sintered sample, the peak corresponding to a single FCC phase was observed in the 1000 °C heat-treated HEA. The patterns inserted in Fig. 1(b) clearly present the phase transformation from two FCC phases to a single FCC phase after heat treatment at 1000 °C.

Microstructures and elemental distribution in HEAs

To investigate the microstructural evolution and elemental distribution after heat treatment, the surface of the as-sintered and 1000 °C heat-treated CoCrCuFeNi HEAs was observed using scanning electron microscopy with energy-dispersive X-ray spectroscopy (SEM-EDS), as shown in Figs. 2 and 3, respectively. Elemental maps of the as-sintered sample (Fig. 2) show two separate CoCrFeNi-rich (named by FCC 1) and Cu-rich phases (named by FCC 2), and the atomic ratio of each phase is listed in Table I. Because Cu has positive mixing enthalpies with other elements, the Cu-rich phase might be separately formed in the alloy [32, 33, 34]. However, after heat treatment at 1000 °C (Fig. 3), CoCuFeNi-rich and Cr oxide are observed in the HEA. The Cr atoms were removed from the CoCrFeNi-rich phase in order to coarsening the Cr₂O₃ during the heat treatment in air atmosphere, and Cu atoms dissolved into the CoFeNi-rich phase. The Gibbs free energy of mixing (ΔG_{mix}) decreases to a negative value with increasing temperature (T , i.e., $\Delta G_{\text{mix}} = \Delta H_{\text{mix}} - T \cdot \Delta S_{\text{conf}}$ where ΔH_{mix} is the mixing enthalpy and ΔS_{conf} is the configuration entropy). Thus, the ability to form a solid solution phase is generally enhanced at high temperatures. Moreover, the thermodynamic calculations based on CALPAD modeling with the TCHEA1 database

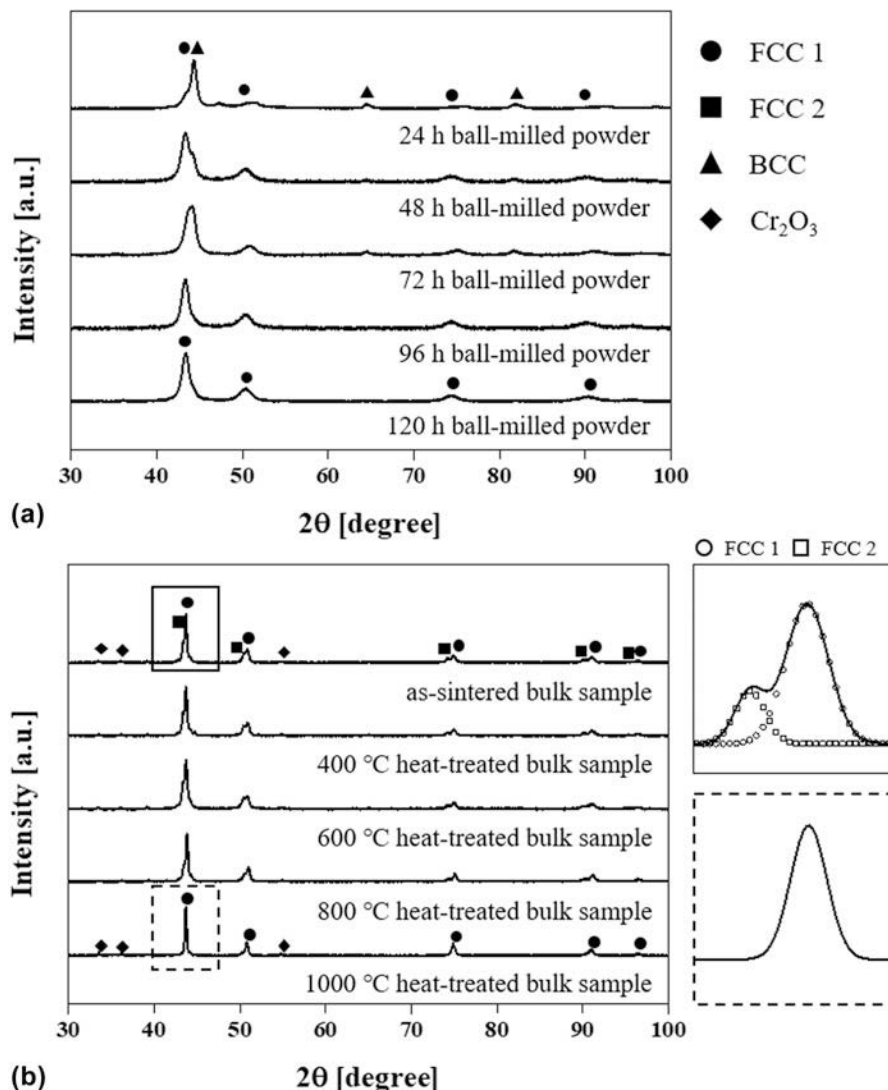


Figure 1: XRD patterns of (a) CoCrCuFeNi powders ball milled for 24, 48, 72, 96, and 120 h, and (b) bulk HEA samples after SPS and heat treatment at 400, 600, 800, and 1000 °C. The inserted patterns in (b) reveal the expended patterns of as-sintered and 1000 °C heat-treated alloys at 2θ range of 42–45°.

[35] also support the transformation of two separate FCC phases to a single solid solution FCC phase at temperatures of >800 °C. Because most Cr atoms were consumed to form Cr precipitates, the composition of the matrix in the HEAs after heat treatment at 1000 °C is similar to that in the CoCuFeNi HEAs. Thus, the XRD results for the 1000 °C heat-treated HEA show a single FCC phase with Cr precipitates, whereas the as-sintered alloy exhibits two separate FCC phases.

The evolution of the CoCrCuFeNi HEA grain size before and after heat treatment was investigated using linear intercept method, which use lines randomly drawn on the transmission electron microscopy (TEM) images. Figure 4 shows TEM images of the as-sintered HEA and alloys heat treated at 400, 600, 800, and 1000 °C. The average grain sizes of the alloys are listed in Table II. The grain size significantly increased from 59 to 386 nm after heat treatment at 1000 °C compared to alloys

heat treated at other temperatures. The degree of grain size increase after heat treatment [i.e., $(D_T - D_0)/D_0 \times 100$, where D_0 is the grain size of the as-sintered HEA and D_T is the grain size of the alloys after heat treatment] is 13.6, 33.9, 69.6, and 554.2% at 400, 600, 800, and 1000 °C, respectively.

Mechanical properties of the CoCrCuFeNi HEAs

Figure 5 shows a comparison of (i) Vickers hardness and (ii) compressive true stress–true strain curves among the as-sintered CoCrCuFeNi HEA and alloys after heat treatment at various temperatures. The measured hardness and yield strength values are listed in Table II. The hardness and yield strength of the as-sintered CoCrCuFeNi HEA reveal high values of 525 Hv and 1920 MPa, respectively, which are superior to FCC phase-based HEAs reported in literatures; CoCrCuFeNi and CoCrFeMnNi HEAs produced via casting

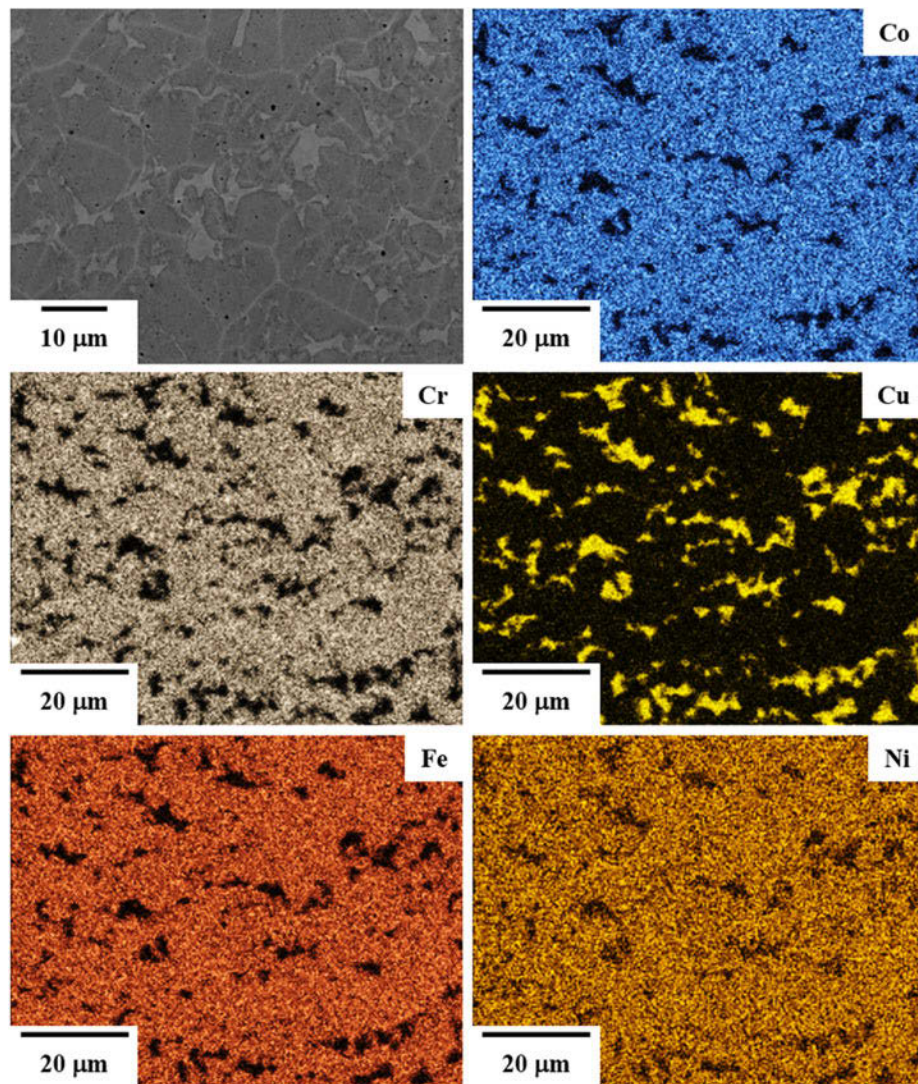


Figure 2: SEM image and elemental maps of the as-sintered CoCrCuFeNi HEA.

exhibit hardness and yield values of 130 Hv and 209 MPa, respectively [1, 36]. However, after heat treatment, the respective values decrease to 262 Hv and 833 MPa with increasing heat treatment temperatures. Moreover, the 400 and 600 °C heat-treated alloys were instantly fractured after yielding because of coarsening the brittle Cr precipitates. Interestingly, plastic strain to failure of the 1000 °C heat-treated alloy increased by approximately 8–32%. This is related to the microstructural evolution of the phases, composition, and grain size after heat treatment. The strengthening and deformation mechanism will be discussed in “Discussion” section, considering the observed microstructural changes in detail.

Discussion

The strengthening and deformation behaviors of the CoCrCu-FeNi HEAs can be discussed with respect to their volume

fraction, composition of each phase, and grain size. The microstructure of the as-sintered and 1000 °C heat-treated alloys was compared to examine the effect of each microstructural parameter on the yield strength of the alloys. The as-sintered HEAs contained two FCC phases (i.e., the CoCrFeNi-rich and Cu-rich phases) and nanoscale grains (59 nm on average), while the heat-treated alloys exhibited a single CoCuFeNi-rich FCC phase and was UFG, with an average size of 386 nm. Because of these microstructural changes, the yield strength decreased from 1920 to 833 MPa after heat treatment.

Strengthening behavior in P/M CoCrCuFeNi HEAs

The mechanical properties of each phase were separately measured using a picoindentation technique, and Fig. 6 summarizes the hardness and elastic moduli of the phases. While all phases exhibit a similar elastic modulus ranging from 130 to

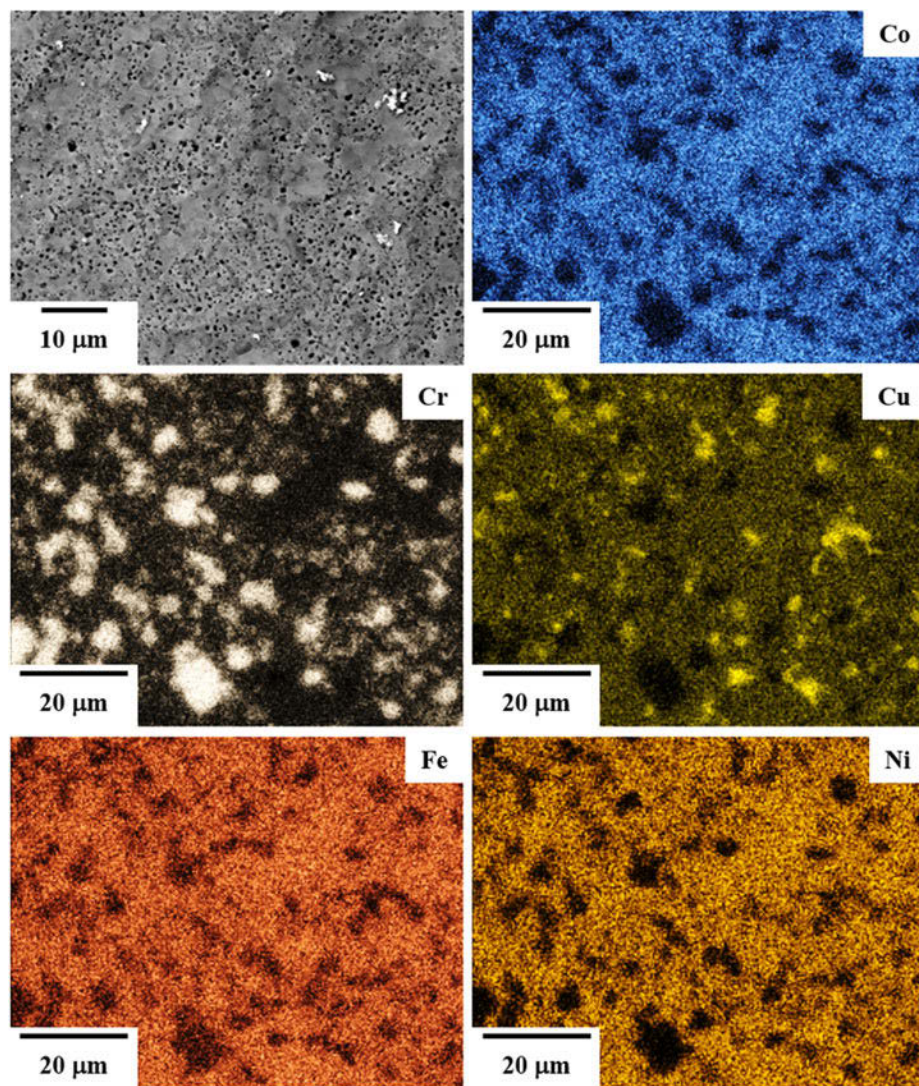


Figure 3: SEM image and elemental maps of 1000 °C heat-treated HEA.

TABLE I: Chemical composition (at.%) of phases in CoCrCuFeNi HEAs.

Sample	Phase	Atomic ratio [at. %]				
		Co	Cr	Cu	Fe	Ni
As SPS	CoCrFeNi rich	22.70	20.19	12.86	22.98	21.28
	Cu rich	8.16	6.66	64.82	8.35	12.02
HT 1000	CoCuFeNi rich	26.16	3.39	20.29	25.13	25.03

140 GPa, the hardness of the CoCrFeNi-rich phase (5.78 GPa) is significantly higher than that of Cu-rich (2.84 GPa) and CoCuFeNi-rich (3.09 GPa) phases. For the as-sintered alloy, the Cu-rich phase was ~12 vol% based on the EDS images, and the hardness was roughly estimated using the rule of mixtures (i.e., $H = H_{\text{CoCrFeNi}} \cdot V_{\text{CoCrFeNi}} + H_{\text{Cu}} \cdot V_{\text{Cu}}$, where H_{phase} and V_{phase} are the hardness and volume fraction of the phase, respectively) as ~5.41 GPa, which is not significantly different from that of the single CoCrFeNi-rich phase (5.78 GPa). Thus,

the significant difference in strength between the as-sintered and heat-treated alloys originates from HEA phases themselves, and the effect of the Cu-rich phase is negligible.

Differences in the degree of lattice distortion and grain size result in significant hardness difference between the CoCrFeNi-rich phase in the as-sintered alloy and CoCuFeNi-rich phase in the heat-treated alloy. Solid solution hardening and grain boundary strengthening are prominent strengthening mechanisms in the HEAs. In solid solution hardening, the strengthening efficiency is related to the degree of lattice distortion, which can be described by the atomic size misfit (δ) as below [37]:

$$\delta = 100 \sqrt{\sum_{i=1}^n x_i (1 - r_i / \bar{r})^2} , \quad (1)$$

where x_i is the content of the i th element and r_i and \bar{r} are atomic radius and average atomic radius of the i th element,

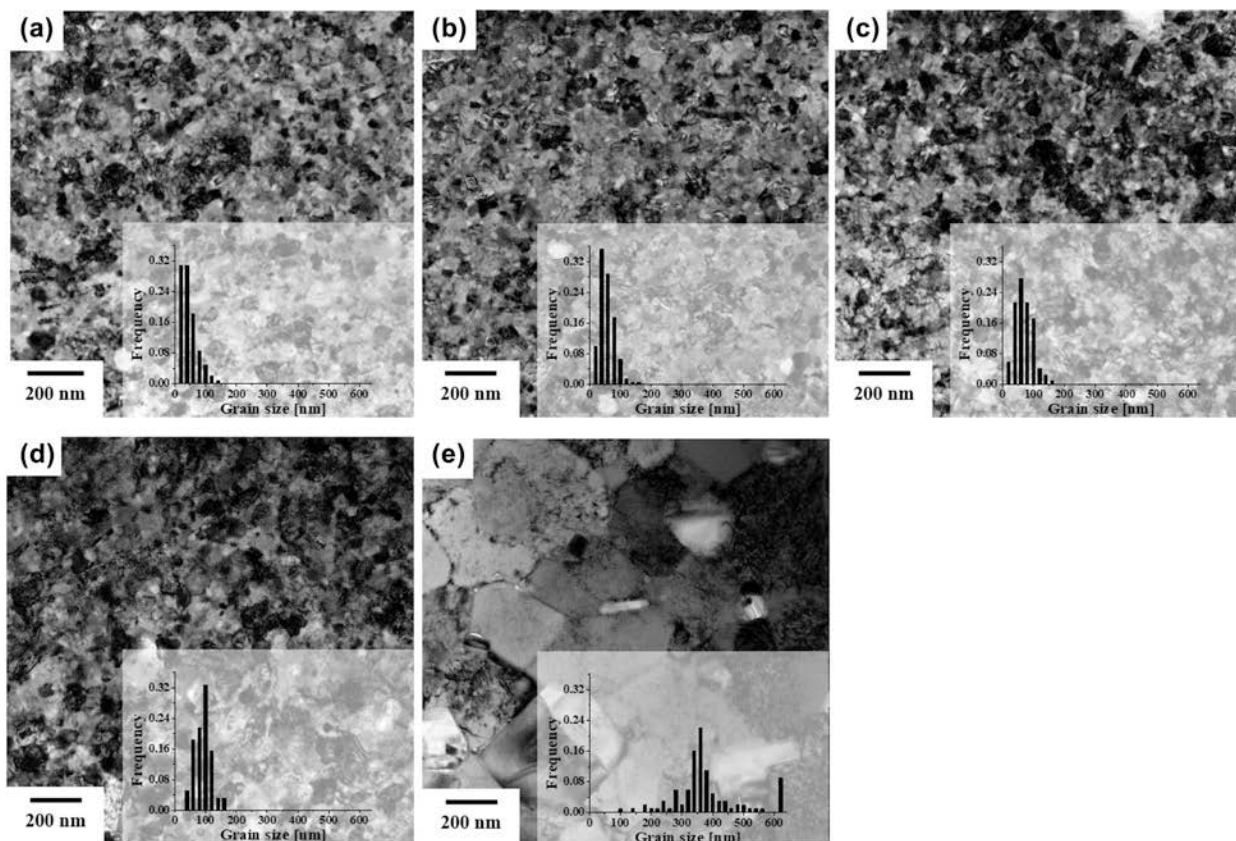


Figure 4: TEM images and grain size distribution of (a) as-sintered HEA and alloys after heat treatment at (b) 400, (c) 600, (d) 800, and (e) 1000 °C.

TABLE II: Summary of grain size, Vickers hardness, and yield strength of as-sintered CoCrCuFeNi and the alloy heat treated (HT) at 400, 600, 800, and 100 °C.

Sample	Grain size (nm)	Vickers hardness (HV)	Yield strength (MPa)
As SPS	59	525	1920
HT 400	67	516	1804
HT 600	79	511	1748
HT 800	100	456	1489
HT 1000	386	262	833

respectively. The atomic size misfit of the as-sintered and 1000 °C heat-treated HEAs was 0.886 and 1.061, respectively, based on the experimentally measured composition (Table I). Since the atomic size of Cu is much larger than that of the other alloying elements, the misfit value increases with increasing Cu concentration. Thus, the solid solution hardening efficiency is higher in the heat-treated HEA than in the as-sintered alloy. However, nanoscale Cu segregates were formed in the grain interior after heat treatment, as shown in Fig. 7, which shows scanning TEM high-angle annular dark-field (STEM-HAADF) image and elemental maps of 1000 °C heat-treated HEA and a certain amount of Cu atoms remained undissolved in the HEA grains. The formation of nanoscale Cu segregates in HEAs has been reported to result in a considerable

loss of solid solution hardening due to reduced lattice strains [38, 39]. Thus, the effect of Cu atoms on lattice distortion in the heat-treated alloy may also be negligible.

The high hardness of the CoCrFeNi-rich HEA phases mainly arises from their small grain size. The grain size of the CoCrCuFeNi HEAs increased from 59 to 386 nm after heat treatment at 1000 °C, while the yield strength of the alloys was reduced from 1920 to 833 MPa. The strengthening effect of grain size (i.e., grain boundary strengthening) in NC and UFG CoCrCuFeNi HEAs can be predicted using the Hall–Petch relationship [40].

$$\sigma_y = \sigma_0 + k_{hp} D^{-1/2} \quad , \quad (2)$$

where σ_y is the yield strength, σ_0 is the intrinsic strength, k_{hp} is the strengthening coefficient, and D is the average grain size. Figure 8 shows the correlation between the yield strength and grain size of the HEAs. The solid and open circles represent data obtained in this study and those reported in literatures [19, 22, 25, 41, 42, 43] (Table III), respectively. Furthermore, the measured strength was compared with theoretical values (marked by lines) calculated using Eq. (2), where the strengthening coefficient for HEAs is listed in Table IV [25, 44]. In this study, the strength matched with the Hall–Petch relationship

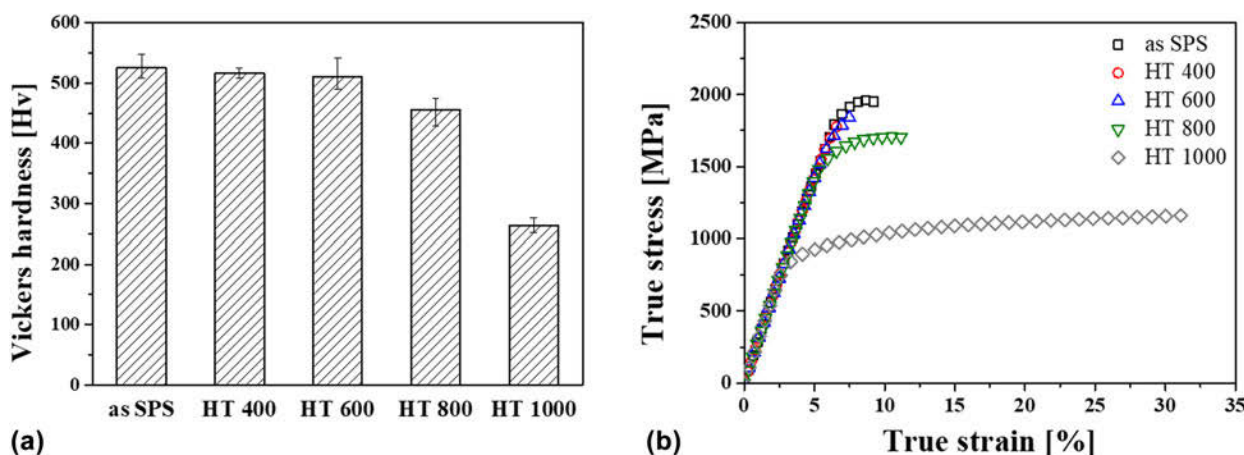


Figure 5: (a) Comparison of Vickers hardness and (b) true strain–true stress curves among as-sintered HEA and alloys after heat-treatment at 400, 600, 800, and 1000 °C.

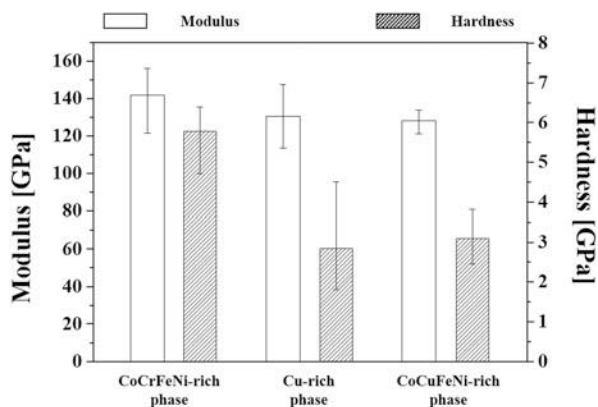


Figure 6: Comparison of elastic modulus and hardness measured on CoCrFeNi-rich and Cu-rich phases in the as-sintered HEA and CoCuFeNi-rich phase in 1000 °C heat-treated HEA.

using a strengthening coefficient of 0.44 MPa m^{1/2}. While the coefficient is similar to the previously reported value for CoCrFeMnNi [25] (0.49 MPa m^{1/2}) evaluated for grain sizes ranging from 503 nm to 88.9 μm, Al_{0.3}CoCrCuFeNi [44] exhibited a high strengthening coefficient value of 0.73 MPa m^{1/2}. Furthermore, the efficiency of grain boundary strengthening in the HEAs was compared with that in NC pure metals with FCC and BCC structures. In general, the strengthening coefficient for metals with a BCC structure (e.g., Cr [45] and Fe [46]) is higher than for those with the FCC phase (e.g., Cu [47] and Ni [48]), as summarized in Table IV. This indicates that the efficiency of boundary strengthening is maximized in BCC metals, as shown in Fig. 8 (marked by dash-line). As the efficiency of grain boundary strengthening is related to the activation of the dislocation source by stress concentration at the grain boundary, the strengthening coefficient can be expressed as function of the shear modulus (G) and Burgers vector (b) of the material, as follows [49]:

$$k_{HP} \approx (\pi m_s \tau_c G b)^{1/2} , \quad (3)$$

where m_s is the microstructural orientation factor and τ_c is the shear stress required for dislocation activation near the grain boundary. Moreover, the coefficient is influenced by the number of available slip systems according to the pile-up model [49, 50]. The slope of the strength variation depending on grain size shows an inverse relationship with the number of slip systems in crystalline materials. Thus, BCC phases may require a large critical shear stress for dislocation propagation at the boundary because of their high shear modulus and limited dislocation slip due to the lower atomic packing fraction compared with FCC phases [45]. However, grain boundary strengthening tends to be more effective in HEAs than their related pure elemental metals, despite adopting the same FCC structure. Because of the significant lattice distortion in HEAs, additional shear stress for dislocation activation is needed to overcome the lattice strain. Hence, the strengthening coefficient of Al_{0.3}CoCrFeNi is higher than those of CoCrCuFeNi and CoCrFeMnNi due to the larger atomic size of Al [25, 45]. Thus, grain boundary strengthening coupled with lattice distortion is a dominant strengthening mechanism in NC and UFG CoCrCuFeNi HEAs.

Deformation mechanism in CoCrCuFeNi HEAs

As previously mentioned, the plastic strain to failure of HEAs increased after heat treatment at 1000 °C. To investigate the deformation behavior in the alloy, TEM specimens were prepared from the heat-treated CoCrCuFeNi HEA after compressive deformation with a strain of 5% at room temperature. Figure 9(a) shows the STEM high-angle annular bright-field (HAABF) image of the deformed alloy and Fig. 9(b) shows the selected area diffraction pattern obtained at the grain

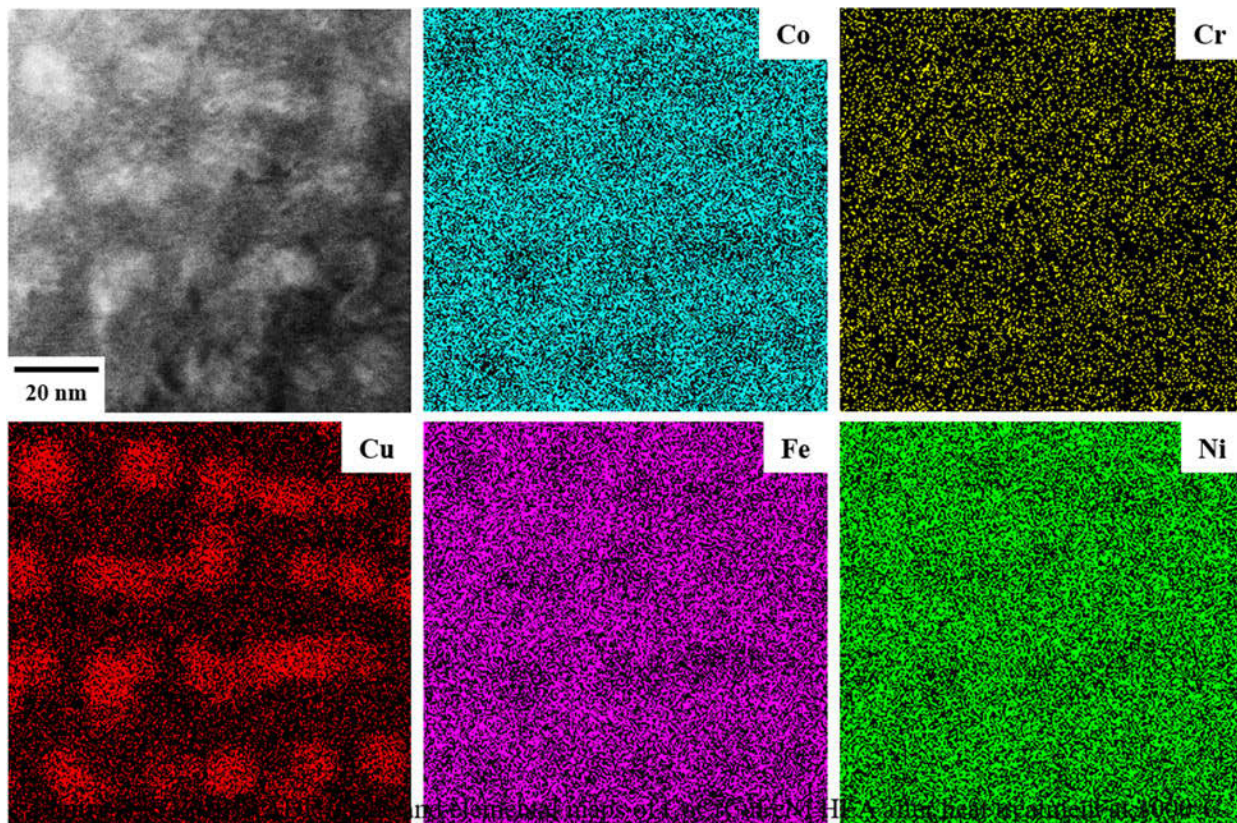


Figure 7: STEM-HAADF image and elemental maps of 1000 °C heat-treated HEA.

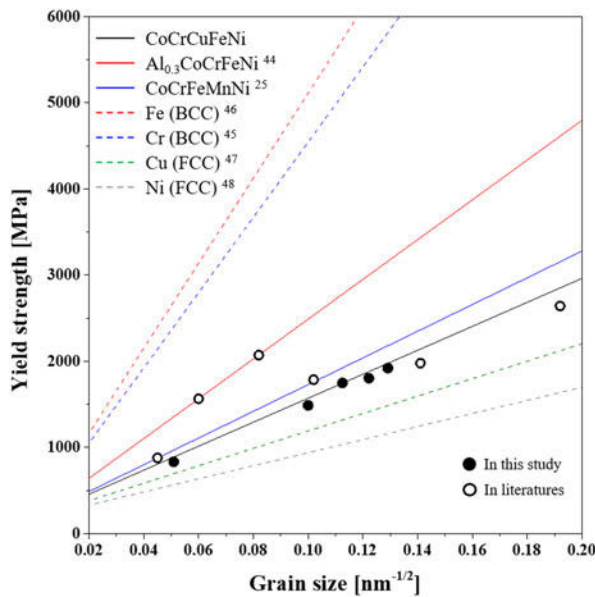


Figure 8: Correlation between yield strength and grain size of HEAs and pure metals measured in this study and reported in literatures.

in Fig. 9(a). The image is the projection for the {011} plane of the alloy. Moreover, two-beam diffraction, the TEM technique used to visualize dislocations as sharp lines with bright contrast in a dark-field (DF) image, was used to observe line defects in

TABLE III: Summary of grain size and yield strength of HEAs reported in literatures.

Composition	Grain size (nm)	Yield strength (MPa)
Al _{0.6} CoCrFeNi _{0.4} [41]	150	2080
Al _{7.5} Co ₂₅ Cu _{17.5} Fe ₂₅ Ni ₂₅ [22]	96	1795
Co _{0.5} CrFeNiTi _{0.5} [42]	27	2650
CoCrFeMnNi [19]	50	1987
CoCrFeMnNi [25]	503	888
CoCrFeMnNi [43]	280	1574

TABLE IV: Summary of strengthening coefficient of HEAs and pure metals calculated in this study and reported in literatures.

Materials	<i>k</i> (MPa m ^{1/2})	
HEA	CoCrCuFeNi	0.44
	Al _{0.3} CoCrFeNi [44]	0.73
	CoCrFeMnNi [25]	0.49
Pure metals	Fe (BCC) [46]	1.56
	Cr (BCC) [45]	1.38
	Cu (FCC) [47]	0.32
	Ni (FCC) [48]	0.24

the alloy. Figures 9(c) and 9(d) show the TEM weak-beam DF images of the grain observed parallel to [011] with diffraction vectors of $g = [111]$ and $g = [200]$, respectively. Dislocations were observed, as marked by white arrows in Figs. 9(c) and 9

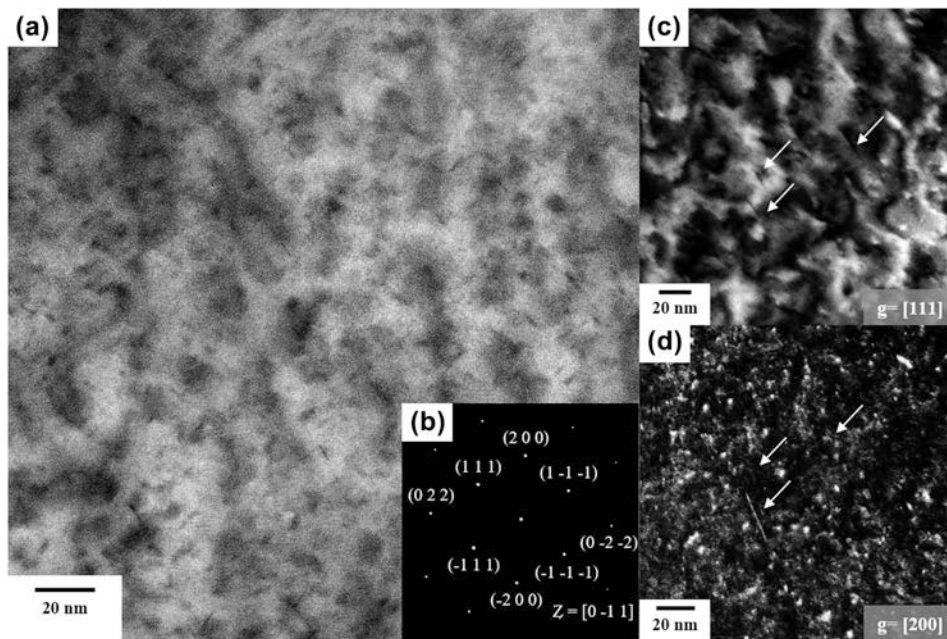


Figure 9: (a) STEM-HAABF image and (b) selected area diffraction pattern and TEM weak-beam DF images observed at (c) $g = [111]$ and (d) $g = [200]$ of 1000 °C heat-treated HEA.

(d). Moreover, the observed dislocation was determined to be an edge dislocation with Burgers vector of $b = [01\bar{1}]$, according to the rule for dislocation analysis [51]. Depending on the composition of the alloys, different deformation mechanisms have been reported according to the stacking fault energy (SFE) of the HEAs [52, 53]. In particular, the deformation behavior of CoCrFeMnNi-based HEAs with low SFEs was determined to be dislocation gliding at the initial plasticity stages, while deformation twinning dominates afterward [54]. However, UFG CoCrCuFeNi HEAs exhibit dislocation gliding as the dominant deformation behavior because their SFEs are higher than those of CoCrFeMnNi. Moreover, the refined microstructure influences the behavior, wherein twinning is more significant in materials with larger grains, as previously reported [55]. The strengthening behavior of CoCrCuFeNi HEAs followed a Hall-Petch relationship, which is related to dislocation pile-up at the grain boundaries. Even though the strength of CoCrCuFeNi HEAs was reduced after heat treatment, the grain growth after heat treatment resulted in improved plastic deformation due to dislocation activation, showing the typical strength–ductility trade-off depending on the grain size.

Conclusion

NC CoCrCuFeNi HEAs were produced via mechanical alloying followed by SPS, and subsequently, heat treatment was performed to produce their UFG HEAs counterparts. The as-sintered HEAs contained two FCC phases (i.e., CoCrFeNi-rich and Cu-rich phases), whereas 1000 °C heat-treated HEA

revealed a single CoCuFeNi-rich phase with an FCC structure. Moreover, the grain size increased from 59 to 386 nm after heat treatment. Consequently, although yield strength decreased from 1930 to 883 MPa, plastic strain to failure increased from 8 to 32% owing to the activation of lattice dislocations. According to microstructural observation, the dominant strengthening mechanism for NC CoCrCuFeNi HEAs can be considered to be grain boundary strengthening. Furthermore, the strengthening coefficient for boundary strengthening of NC HEA was higher than that in the corresponding pure elemental metals with FCC structure owing to its significant lattice distortion.

Experimental procedure

CoCrCuFeNi HEAs, with a wide range of grain sizes from 59 to 386 nm, were produced by annealing P/M HEAs produced via ball milling followed by SPS. First, a hand mixed blend of Co, Cr, Cu, Fe, and Ni powders (all powders with >99.5% purity, supplied by Sigma-Aldrich Korea Co., Ltd., Yongin, Korea) with equiatomic ratio was mechanically alloyed using an attrition mill (AT-01; Daewha tech Co., Ltd., Yongin, Korea). Stainless steel balls of 5 mm diameter were utilized as the milling media with a ball-to-powder ratio of 10:1, and 2 wt% stearic acid [$\text{CH}_3(\text{CH}_2)_{16}\text{CO}_2\text{H}$; Sigma Aldrich Korea Co., Ltd., Yongin, Korea] was used as a process control agent to prevent powder agglomeration during milling. The blend powder, balls, and stearic acid were placed into a stainless steel chamber. To prevent the increase of internal temperature during milling,

cooling water was circulated through the wall of the chamber. High-energy ball milling was performed at 600 rpm for 24, 48, 72, 96, and 120 h under an Ar atmosphere. After milling, the stearic acid was burned off at 500 °C for 30 min for the subsequent sintering process. The ball-milled powder was sintered into a pellet using SPS (JM-SPS-025; Vacuum Science Laboratory, Seoul, Korea). The ball-milled powder was placed in a graphite mold with a 30-mm-diameter cylindrical inner cavity, and sintering was conducted at 800 °C for 10 min under a uniaxial pressure of 75 MPa and vacuum of 60 mtorr. Finally, the specimens were heat treated at 400, 600, and 1000 °C for 72 h using a laboratory chamber furnace (ECF 12/6; Lenton Furnaces Ltd., Hope Valley, UK) in air to investigate the microstructural and mechanical evolution after heat treatment.

Phase identification was performed on the ball-milled powders and the as-sintered and heat-treated HEAs using XRD (Smartlab; Rigaku, Tokyo, Japan) with Cu K α radiation at 1.5406 Å. Field-emission SEM (Verios 460L, FEI, Hillsboro, Oregon) with EDS (EDAX-AMETEK, Mahwah, NJ) was used to observe the surface morphology and elemental distribution of the sintered HEAs. Microstructures of the HEAs were characterized using a high-resolution transmission electron microscopy (Tecnai G2 F20, FEI, Hillsboro, Oregon) system operated at 200 kV. The TEM samples were prepared using a dual-beam focused ion beam SEM (Helios NanoLab 650, FEI, Hillsboro, Oregon). To evaluate the mechanical property of the alloys, Vickers hardness tests (HM-200; Mitutoyo, Kawasaki, Japan) were performed on the fine-polished samples under an applied load of 0.5 kgf. The hardness and elastic moduli of the phases formed in the as-sintered sample were compared using *in situ* SEM picoindentation tests (PI-87; Hysitron Inc., Minneapolis, MN) with a cube-corner probe till an indentation depth of 700 nm. Compression tests were performed for samples with a size of 2 × 2 × 3 mm³ at a strain rate of 10⁻⁴ s⁻¹ using a universal testing machine (RB Model 301 Unitech M; R&B Inc.).

Acknowledgment

This study was supported by the National Research Foundation (NRF) of Korea and funded by Ministry of Science, ICT (MSIT; 2013K1A4A3055679, 2015R1D1A1A01060718, 2015R1A5A7037615, 2016M2B2A9A02943809, and 2017M1A3A3A02015639).

References

- J.W. Yeh, S.K. Chen, S.J. Lin, J.Y. Gan, T.S. Chin, T.T. Shun, C.H. Tsau, and S.Y. Chang:** Nanostructured high-entropy alloys with multiple principal elements: Novel alloy design concepts and outcomes. *Adv. Eng. Mater.* **6**, 299 (2004).
- B. Gwalani, V. Soni, D. Choudhuri, M. Lee, J.Y. Hwang, S.J. Nam, H. Ryu, S.H. Hong, and R. Banerjee:** Stability of ordered L₁₂ and B₂ precipitates in face centered cubic based high entropy alloys—Al_{0.3}CoFeCrNi and Al_{0.3}CuFeCrNi₂. *Scr. Mater.* **123**, 130 (2016).
- M.H. Tsai, H. Yuan, G. Cheng, W. Xu, K.Y. Tsai, C.W. Tsai, W.W. Jian, C.C. Juan, W.J. Shen, M.H. Chuang, J.W. Yeh, and Y.T. Zhu:** Morphology, structure and composition of precipitates in Al_{0.3}CoCrCu_{0.5}FeNi high-entropy alloy. *Intermetallics* **32**, 329 (2013).
- X.F. Wang, Y. Zhang, Y. Qiao, and G.L. Chen:** Novel microstructure and properties of multicomponent CoCrCuFeNiTi_x alloys. *Intermetallics* **15**, 357 (2007).
- C-J. Tong, Y-L. Chen, J-W. Yeh, S-J. Lin, S-K. Chen, T-T. Shun, C-H. Tsau, and S-Y. Chang:** Microstructure characterization of Al_xCoCrCuFeNi high-entropy alloy system with multiprincipal elements. *Metall. Mater. Trans. A* **36**, 881 (2005).
- A. Kumar, P. Dhekne, A.K. Swarnakar, and M.K. Chopkar:** Analysis of Si addition on phase formation in AlCoCrCuFeNiSi_x high entropy alloys. *Mater. Lett.* **188**, 73 (2017).
- T. Borkar, B. Gwalani, D. Choudhuri, C.V. Mikler, C.J. Yannetta, X. Chen, R.V. Ramanujan, M.J. Styles, M.A. Gibson, and R. Banerjee:** A combinatorial assessment of Al_xCrCuFeNi₂ (0 < x < 1.5) complex concentrated alloys: Microstructure, microhardness, and magnetic properties. *Acta Mater.* **116**, 63 (2016).
- H. Jiang, K. Han, D. Qiao, Y. Lu, Z. Cao, and T. Li:** Effects of Ta addition on the microstructures and mechanical properties of CoCrFeNi high entropy alloy. *Mater. Chem. Phys.* **210**, 43 (2018).
- W.H. Liu, T. Yang, and C.T. Liu:** Precipitation hardening in CoCrFeNi-based high entropy alloys. *Mater. Chem. Phys.* **210**, 2 (2018).
- C.C. Koch:** Nanocrystalline high-entropy alloys. *J. Mater. Res.* **32**, 3435 (2017).
- Y. Zou, J.M. Wheeler, H. Ma, P. Okle, and R. Spolenak:** Nanocrystalline high-entropy alloys: A new paradigm in high-temperature strength and stability. *Nano Lett.* **17**, 1569 (2017).
- H. Shahmir, J. He, Z. Lu, M. Kawasaki, and T.G. Langdon:** Effect of annealing on mechanical properties of a nanocrystalline CoCrFeNiMn high-entropy alloy processed by high-pressure torsion. *Mater. Sci. Eng., A* **676**, 294 (2016).
- P.F. Yu, H. Cheng, L.J. Zhang, H. Zhang, Q. Jing, M.Z. Ma, P.K. Liaw, G. Li, and R.P. Liu:** Effects of high pressure torsion on microstructures and properties of an Al_{0.1}CoCrFeNi high-entropy alloy. *Mater. Sci. Eng., A* **655**, 283 (2016).
- S. Nam, M.J. Kim, J.Y. Hwang, and H. Choi:** Strengthening of Al_{0.15}CoCrCuFeNiTi_x-C (x = 0, 1, 2) high-entropy alloys by grain refinement and using nanoscale carbides via powder metallurgical route. *J. Alloys Compd.* **762**, 29 (2018).

15. R.S. Ganji, P. Sai Karthik, K. Bhanu Sankara Rao, and K.V. Rajulapati: Strengthening mechanisms in equiatomic ultrafine grained AlCoCrCuFeNi high-entropy alloy studied by micro- and nanoindentation methods. *Acta Mater.* **125**, 58 (2017).
16. D-H. Lee, I-C. Choi, M-Y. Seok, J. He, Z. Lu, J-Y. Suh, M. Kawasaki, T.G. Langdon, and J. Jang: Nanomechanical behavior and structural stability of a nanocrystalline CoCrFeNiMn high-entropy alloy processed by high-pressure torsion. *J. Mater. Res.* **30**, 2804 (2015).
17. B. Schuh, F. Mendez-Martin, B. Völker, E.P. George, H. Clemens, R. Pippan, and A. Hohenwarter: Mechanical properties, microstructure and thermal stability of a nanocrystalline CoCrFeMnNi high-entropy alloy after severe plastic deformation. *Acta Mater.* **96**, 258 (2015).
18. H. Shahmir, T. Mousavi, J. He, Z. Lu, M. Kawasaki, and T.G. Langdon: Microstructure and properties of a CoCrFeNiMn high-entropy alloy processed by equal-channel angular pressing. *Mater. Sci. Eng., A* **705**, 411 (2017).
19. W. Ji, W. Wang, H. Wang, J. Zhang, Y. Wang, F. Zhang, and Z. Fu: Alloying behavior and novel properties of CoCrFeNiMn high-entropy alloy fabricated by mechanical alloying and spark plasma sintering. *Intermetallics* **56**, 24 (2014).
20. W. Chen, Z. Fu, S. Fang, H. Xiao, and D. Zhu: Alloying behavior, microstructure and mechanical properties in a FeNiCr_{0.3}Al_{0.7} high entropy alloy. *Mater. Des.* **51**, 854 (2013).
21. H.J. Fecht, E. Hellstern, Z. Fu, and W.L. Johnson: Nanocrystalline metals prepared by high-energy ball milling. *Metall. Trans. A* **21**, 2333 (1990).
22. Z. Fu, W. Chen, H. Wen, D. Zhang, Z. Chen, B. Zheng, Y. Zhou, and E.J. Lavernia: Microstructure and strengthening mechanisms in an FCC structured single-phase nanocrystalline Co₂₅Ni₂₅Fe₂₅Al_{7.5}Cu_{17.5} high-entropy alloy. *Acta Mater.* **107**, 59 (2016).
23. C.C. Koch, D.G. Morris, K. Lu, and A. Inoue: Ductility of nanostructured materials. *MRS Bull.* **24**, 54 (1999).
24. H. Van Swygenhoven and J.R. Weertman: Deformation in nanocrystalline metals. *Mater. Today* **9**, 24 (2006).
25. S.J. Sun, Y.Z. Tian, H.R. Lin, X.G. Dong, Y.H. Wang, Z.J. Zhang, and Z.F. Zhang: Enhanced strength and ductility of bulk CoCrFeMnNi high entropy alloy having fully recrystallized ultrafine-grained structure. *Mater. Des.* **133**, 122 (2017).
26. E. Ma and T. Zhu: Towards strength-ductility synergy through the design of heterogeneous nanostructures in metals. *Mater. Today* **20**, 323 (2017).
27. X. Wu, F. Yuan, M. Yang, P. Jiang, C. Zhang, L. Chen, Y. Wei, and E. Ma: Nanodomained nickel unite nanocrystal strength with coarse-grain ductility. *Sci. Rep.* **5**, 11728 (2015).
28. Z. Li, K.G. Pradeep, Y. Deng, D. Raabe, and C.C. Tasan: Metastable high-entropy dual-phase alloys overcome the strength-ductility trade-off. *Nature* **534**, 227 (2016).
29. C. Suryanarayana: Mechanical alloying and milling mechanical engineering. *Prog. Mater. Sci.* **46**, 1 (2001).
30. X. Yang and Y. Zhang: Prediction of high-entropy stabilized solid-solution in multi-component alloys. *Mater. Chem. Phys.* **132**, 233 (2012).
31. S. Guo, C. Ng, J. Lu, and C.T. Liu: Effect of valence electron concentration on stability of fcc or bcc phase in high entropy alloys. *J. Appl. Phys.* **109**, 103505 (2011).
32. F.R. Boer: *Cohesion in Metals: Transition Metal Alloys* (North-Holland, Amsterdam, 1988).
33. H.F. Sheng, M. Gong, and L.M. Peng: Microstructural characterization and mechanical properties of an Al_{0.5}CoCrFeCuNi high-entropy alloy in as-cast and heat-treated/quenched conditions. *Mater. Sci. Eng., A* **567**, 14 (2013).
34. T. Guo, J. Li, J. Wang, Y. Wang, H. Kou, and S. Niu: Liquid-phase separation in undercooled CoCrCuFeNi high entropy alloy. *Intermetallics* **86**, 110 (2017).
35. H. Mao, H-L. Chen, and Q. Chen: TCHEA1: A thermodynamic database not limited for "High entropy" alloys. *J. Phase Equilib. Diffus.* **38**, 353 (2017).
36. J.Y. He, W.H. Liu, H. Wang, Y. Wu, X.J. Liu, T.G. Nieh, and Z. P. Lu: Effects of Al addition on structural evolution and tensile properties of the FeCoNiCrMn high-entropy alloy system. *Acta Mater.* **62**, 105 (2014).
37. S. Fang, X. Xiao, L. Xia, W. Li, and Y. Dong: Relationship between the widths of supercooled liquid regions and bond parameters of Mg-based bulk metallic glasses. *J. Non-Cryst. Solids* **321**, 120 (2003).
38. X.D. Xu, P. Liu, S. Guo, A. Hirata, T. Fujita, T.G. Nieh, C. T. Liu, and M.W. Chen: Nanoscale phase separation in a fcc-based CoCrCuFeNiAl_{0.5} high-entropy alloy. *Acta Mater.* **84**, 145 (2015).
39. R. Sonkusare, P.D. Janani, N.P. Gurao, S. Sarkar, S. Sen, K. G. Pradeep, and K. Biswas: Phase equilibria in equiatomic CoCuFeMnNi high entropy alloy. *Mater. Chem. Phys.* **210**, 269 (2018).
40. T.H. Courtney: *Mechanical Behavior of Materials* (Waveland Press, Long Grove, 2005).
41. Z. Fu, W. Chen, S. Fang, D. Zhang, H. Xiao, and D. Zhu: Alloying behavior and deformation twinning in a CoNiFeCrAl_{0.6}Ti_{0.4} high entropy alloy processed by spark plasma sintering. *J. Alloys Compd.* **553**, 316 (2013).
42. Z. Fu, W. Chen, H. Xiao, L. Zhou, D. Zhu, and S. Yang: Fabrication and properties of nanocrystalline Co_{0.5}FeNiCrTi_{0.5} high entropy alloy by MA-SPS technique. *Mater. Des.* **44**, 535 (2013).
43. S-H. Joo, H. Kato, M.J. Jang, J. Moon, E.B. Kim, S-J. Hong, and H.S. Kim: Structure and properties of ultrafine-grained CoCrFeMnNi high-entropy alloys produced by mechanical alloying and spark plasma sintering. *J. Alloys Compd.* **698**, 591 (2017).

44. S.G. Ma, S.F. Zhang, J.W. Qiao, Z.H. Wang, M.C. Gao, Z.M. Jiao, H.J. Yang, and Y. Zhang: Superior high tensile elongation of a single-crystal CoCrFeNiAl_{0.3} high-entropy alloy by Bridgman solidification. *Intermetallics* **54**, 104 (2014).
45. D. Wu, J. Zhang, J.C. Huang, H. Bei, and T.G. Nieh: Grain-boundary strengthening in nanocrystalline chromium and the Hall-Petch coefficient of body-centered cubic metals. *Scr. Mater.* **68**, 118 (2013).
46. A.S. Khan, H. Zhang, and L. Takacs: Mechanical response and modeling of fully compacted nanocrystalline iron and copper. *Int. J. Plast.* **16**, 1459 (2000).
47. J. Chen, L. Lu, and K. Lu: Hardness and strain rate sensitivity of nanocrystalline Cu. *Scr. Mater.* **54**, 1913 (2006).
48. A. Godon, J. Creus, S. Cohendoz, E. Conforto, X. Feaugas, P. Girault, and C. Savall: Effects of grain orientation on the Hall-Petch relationship in electrodeposited nickel with nanocrystalline grains. *Scr. Mater.* **62**, 403 (2010).
49. R. Armstrong, I. Codd, R.M. Douthwaite, and N.J. Petch: The plastic deformation of polycrystalline aggregates. *Philos. Mag.* **7**, 45 (1962).
50. A.C. Arko and Y.H. Liu: The effect of atomic order on the Hall-Petch behavior in Ni₃Fe. *Metall. Trans.* **2**, 1875 (1971).
51. D.B. Williams and C.B. Carter: *The Transmission Electron Microscope. Transmission Electron Microscopy* (Springer, New York, 1996).
52. G. Laplanche, A. Kostka, O.M. Horst, G. Eggeler, and E.P. George: Microstructure evolution and critical stress for twinning in the CrMnFeCoNi high-entropy alloy. *Acta Mater.* **118**, 152 (2016).
53. J. Liu, C. Chen, Y. Xu, S. Wu, G. Wang, H. Wang, Y. Fang, and L. Meng: Deformation twinning behaviors of the low stacking fault energy high-entropy alloy: An in situ TEM study. *Scr. Mater.* **137**, 9 (2017).
54. F. Otto, A. Dlouhy, C. Somsen, H. Bei, G. Eggeler, and E.P. George: The influences of temperature and microstructure on the tensile properties of a CoCrFeMnNi high-entropy alloy. *Acta Mater.* **61**, 5743 (2013).
55. S.W. Wu, G. Wang, J. Yi, Y.D. Jia, I. Hussain, Q.J. Zhai, and P.K. Liaw: Strong grain-size effect on deformation twinning of an Al_{0.1}CoCrFeNi high-entropy alloy. *Mater. Res. Lett.* **5**, 276 (2017).